J Mater Sci: Mater Electron (2015) 26:4226–4233
DOI 10.1007/s10854-015-2972-9

Synthesis and characterization of VO_2(B)/graphene nanocomposite for supercapacitors

Xuxian Xiao[1] · Shun Li[1] · Hua Wei[2] · Dan Sun[1] · Yuanzhan Wu[1] · Guizhen Jin[1] · Fen Wang[1] · Yingping Zou[1]

Received: 26 January 2015 / Accepted: 16 March 2015 / Published online: 1 April 2015

Abstract A hydrothermal method assisted with freeze drying process was adopted to form composite supercapacitor materials of metastable vanadium dioxide [VO_2(B)] nanobelts on reduced graphene oxide (RG) layers. The VO_2(B) nanobelts were well dispersed on the graphene layers as verified by scanning electron microscopy and high-resolution transmission electron microscope. Cyclic voltammetry and galvanostatic charge–discharge measurements were adopted to investigate the electrochemical properties of VO_2(B)/RG composites in 1.0 M Na_2SO_4 aqueous solution. The VO_2(B)/RG composites delivered better specific capacitance and superior rate capability in comparison with the pure VO_2(B). The initial specific capacitance of the composites reached 290.4 F g^{-1} at 0.2 A g^{-1} and maintained 82.3 % of the initial value after 1000 cycles at 2 A g^{-1}, 37.9 % higher than the pure VO_2(B). Therefore, our results suggest that graphene greatly enhances the electrochemical performance of VO_2(B) and VO_2(B)/RG composite is a potential material for supercapacitor.

1 Introduction

Supercapacitors, also known as electrochemical capacitors or ultracapacitors, have drawn tremendous attention as an energy storage in composite electric vehicles, memory back-up devices, large industrial equipment, and renewable energy power plants [1, 2] due to their unique superiority such as fast charge–discharge rate, long cycling life, and good safety [3, 4]. They are usually defined into electrochemical double-layer capacitance (EDLC) with carbon based electrodes and pseudo-capacitance with transition metal oxides as well as conducting polymers electrodes [5, 6]. However, the EDLC only delivers the theory specific capacitance (150 F g^{-1}) and energy density (3–5 Wh kg^{-1}) in liquid electrolytes (aqueous an alkali) due to their limiting factor of low water decomposition potential of 1.23 V [7]. Recently, transitional metal oxides have attracted significant attention for pseudo-capacitance since they could offer higher capacitance than pure carbon materials as well as longer cycle life than conductive polymers [8–10].

Among transition metal oxides, vanadium oxides, which contain metal atoms capable of various valence states, are one of the most promising electrode materials for commercial supercapacitors due to their relatively high energy density, ease of synthesis, low cost, and abundant resources [11, 12]. As an important functional metal oxide, vanadium dioxide possesses excellent physical and chemical properties. Nevertheless, the poor electrical conductivity and structural stability of VO_2(B) have hindered its application for high power and long-term cycling electrochemical capacitors [11–13]. To improve the capacitive performance, it is of great importance to enhance the electrical conductivity and structural stability of VO_2(B) and maintain high electrolyte penetration/diffusion rates. Based on this, many strategies, such as composite technology, doping, size tailoring and so on [14–16], have been proposed. Among them, the composite technology, which is combining some materials with good electrical conductivity and structural stability with redox active vanadium oxides, may be an

✉ Xuxian Xiao
308558692@qq.com

✉ Yingping Zou
lshlj205@163.com

[1] College of Chemistry and Chemical Engineering, Central South University, Changsha 410083, China

[2] College of Life Science, Jiangxi Science and Technology Normal University, Jiangxi 330038, China

effective strategy to improve the capacity and cycling stability. In addition, preparing special structure of vanadium dioxide is a generic method. Various VO_2(B) nanostructures such as nanowires [17], monodisperse spheres [18], nanobelts [19] and nanoparticles [20], have been synthesized and applied in lithium ion battery. However, VO_2(B) nanobelt as the electrode material for supercapacitors is seldomly reported so far. A composite of VO_2(B) with ordered mesoporous carbon was once prepared by a solid-state reaction and delivered a capacitance of about 131 F g^{-1} in 1 M KNO_3 solution [21]. And VO_2(B)/CNTs composite shows a specific capacitance of 250 F g^{-1} in 1 M Na_2SO_4 solution at a current density of 0.5 A g^{-1} [14]. Even though the results of relatively lower capacitance or lower stability are far from meeting the need of commercial application. The facile synthesis of VO_2(B) composite for improving the electrochemical property is eagerly required.

Graphene, a flat monolayer of carbon atoms tightly packed into a two-dimensional (2D) honeycomb lattice [22, 23], showed many superiorities in mechanical, electronical (with carrier mobility up to 200,000 cm^2 V^{-1} s^{-1}) [24, 25], and thermal conductivity (4840–5300 W m^{-1} K^{-1}) [26]. Moreover, graphene possess a specific surface area ($\sim$2630 m^2 g^{-1}) [27] for improving interfacial contact. The graphene wrapping process greatly improves electronic interparticle connection and prevents agglomeration during cycling. There are many studies on graphene as composites such as graphene/MnO_2 [28], graphene/Co_3O_4 [29], graphene/Ni$(OH)_2$ [30], graphene/Fe_3O_4 [31] for supercapacitors, and they show a great breakthrough for enhancing electronic performance of bare metal oxides. Currently, Deng et al. [32] synthesized graphene composites with starfruit-like VO_2(B) particles, of which the capacitance was 225 F g^{-1} in 0.5 M K_2SO_4 at 0.25 A g^{-1}. However, the performance is still disappointing and it is still a big challenge to develop a simple and rapid approach to synthesize VO_2(B)/graphene composites with better performance.

In this study, VO_2(B) nanobelts were homogeneously embedded into the graphene nanosheets by one step hydrothermal process in which the graphite oxide (GO) were reduced to graphene (RG) without using any toxic organic solvent. Besides, to obtain the porous and loose morphology, we take special drying. The freeze drying process is more effective than previously reported in maintaining the microstructure of the materials. The VO_2(B)/RG composite exhibited good electrochemical properties in 1 mol L^{-1} Na_2SO_4 solution in comparison with previously reported, which is probably due to the as-fabricated graphene sheets in the composites have lower defects, better distribution and higher reduction.

2 Experimental methods

2.1 Materials and sample preparation

All chemical reagents used in this experiment were analytical grade without any further purification. Graphite oxide (GO) was synthesized from natural graphite flakes by a modified Hummers method [33]. The suspension of GO was prepared by ultrasonication of 35 mg GO in 35 ml distilled water for 30 min. 0.2115 g of V_2O_5 and 0.2909 g of oxalic acid were dissolved in the GO suspension by stirring for 15 min. The mixed solution was heated to 60 °C in an oil bath with vigorously stirring for 1 h, then the dispersion was transferred into a 50 ml Teflon- lined stainless steel autoclave and was maintained at 180 °C for 24 h. After the solution was naturally cooled to room temperature, the black product was collected and washed with distilled water and ethanol for several times, and then freeze drying for 12 h, and the final product was denoted as VO_2(B)/RG(1.0). In other two experiments, the as-synthesized precipitates with 0.5 mg ml^{-1} GO and 2.0 mg ml^{-1} GO were designated as VO_2(B)/RG(0.5) and VO_2(B)/RG(2.0), respectively. For comparison, reduced graphite oxide (RG) and pure VO_2(B) were prepared with the similar method.

2.2 Materials characterizations

The phase of as-synthesized samples was checked by a MXPAHF X-ray diffractometer from 10° to 80° with Cu Kα radiation ($\lambda = 1.54056$ Å). Thermogravimetric analysis (TGA) was performed on a thermogravimeter analyzer (TGA, DTA-50, Shimazu, Japan) from room temperature to 700 °C at a heating rate of 10 °C min^{-1} in air flux. Fourier transform infrared (FT-IR) spectra of the samples were recorded on a VECTOR-22 (Bruker) spectrometer with KBr pellet and the effective range was from 400 to 4000 cm^{-1}. X-ray photoelectron spectroscopy (XPS) was done with a Thermo VG Scientific SiRGa Probe spectrometer. The morphology was observed by using field-emission scanning electron microscopy (FE-SEM, FEI Nova Nano-230) and high-resolution transmission electron microscope (HR-TEM, JEOL-2010).

2.3 Electrochemical measurements

The electrochemical performances of the synthesized composite materials and pure VO_2(B) nanobelts were measured by a conventional three-electrode cell. The working electrodes were fabricated by pressing a mixture of the active materials, acetylene black, and polytetrafluoroethylene (PTFE, 10 wt%) at a weight ratio of

80:10:10 onto a stainless foil (1 × 1 cm) which served as a current collector, and dried in a vacuum oven at 70 °C overnight. The counter electrode and reference electrode were a platinum sheet and a saturated calomel electrode (SCE), respectively. 1 M Na_2SO_4 solution was used as the electrolyte. Cyclic voltammetry (CV) and galvanostatic charge–discharge tests were investigated in a voltage window from −0.4 to 0.6 V on a CHI660B electrochemical workstation (Shanghai, China) at ambient temperature. Electrochemical impedance spectroscopy (EIS) measurements were performed on a P2273 electrochemical workstation (Princeton Applied Research, USA) and the frequency range applied was 0.01 Hz–100 kHz with an AC amplitude of 5 mV.

3 Results and discussion

3.1 Structure characterization

Figure 1 shows the XRD patterns of GO (a), RG (b), bare VO_2(B) (c), and VO_2(B)/RG composite (d). As shown in Fig. 1a, the precursor GO is dominated by a single broad peak at 10.3°, which corresponds to an interlayer distance of 0.83 nm. The larger interlayer distance relative to the initial graphite ($d_{002} = 0.34$ nm) is consistent with the oxidation of graphite and intercalation of water. After hydrothermal treatment, the broad peak (Fig. 1b) between 22° and 24° could be ascribed to the disordered RG layers, indicating the graphene sheets formed [34]. The pure VO_2(B) and VO_2(B)/RG composite are presented in Fig. 1c, d in which the main diffraction peaks can be indexed to the monoclinic VO_2(B) with lattice constants $a = 12.027$ Å, $b = 3.710$ Å, and $c = 6.570$ Å and $\beta = 108.7$ Å (JCPDS Card No. 65-7960). The result shows that no impurity phase exists in the VO_2(B). Meanwhile, the peak (002) at 24° (Fig. 1d) becomes broad and strong in comparison with the pure VO_2(B) (Fig. 1c), suggesting the presence of largely exfoliated graphene layers [35].

Figure 2 shows the FT-IR spectra of GO, and VO_2(B)/RG. In the FT-IR spectrum of GO (Fig. 2a), stretches of O–H, C=O, aromatic C=C, carboxyl C–O, and alkoxy can be clearly identified at 3400, 1722, 1620, 1410, and 1060 cm^{-1}, respectively, which is consistent with previous report [36]. However, all these absorption peaks related to the oxygen-containing functional groups become very weak or entirely disappeared (carboxyl groups are considerably decreased) in the FT-IR spectra of the VO_2(B)/RG composite (Fig. 2b) remains, suggesting that the high purity of graphene can be achieved [37, 38]. In addition, the appearance of two new absorption peaks at about 540 cm^{-1} and 1000 cm^{-1} in the FT-IR spectrum, which relates to V–O–V and V=O vibrations, implies the existence of vanadium oxide [39]. Thus, the FT-IR results further confirm the formation of VO_2(B) and the reduction of GO.

XPS method was applied to accurately determine the composition and valence state of V of the composite. XPS spectrum of VO_2(B)/RG(1.0) is displayed in Fig. 3 and shows that all elements such as carbon, oxygen, and vanadium can be indexed on the surface of the sample (Fig. 3a). The C1s core-level spectrum (Fig. 3b) shows non-oxygenated carbon, carbon in C–O (sp2-compositeized

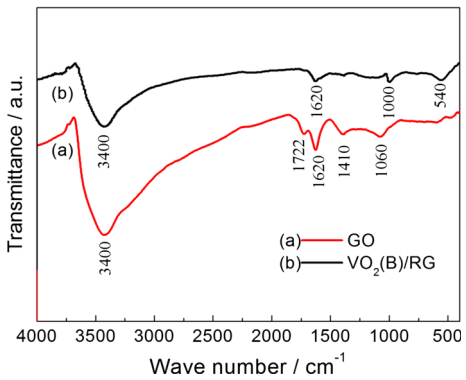

Fig. 2 FT-IR spectra of GO (*a*) and VO_2(B)/RG (*b*)

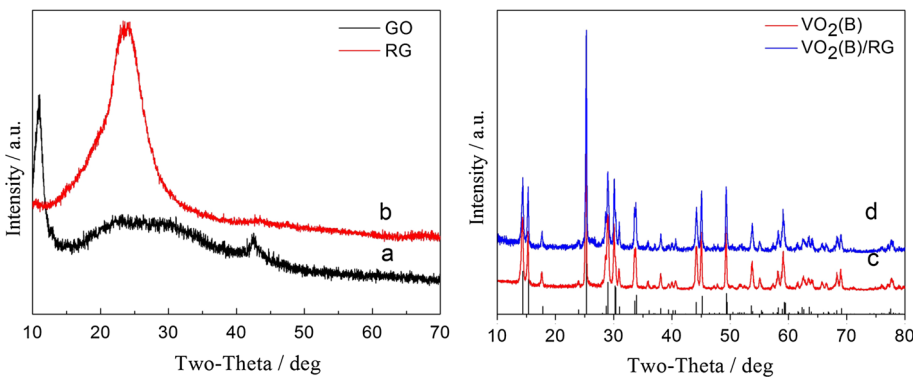

Fig. 1 XRD patterns of GO (*a*), reduced graphene oxide (RG) (*b*), pure VO_2(B) (*c*) and VO_2(B)/RG (*d*)

carbon), C=O (carbonyl groups) and O–C=O (carboxyl groups) at 284.6, 285.7, 286.6 and 288.5 eV, respectively. The relatively smaller intensities of these peaks indicate the reduction of GO [40]. From this result, it can be concluded that the hydroxyl functional groups are mostly presented on VO_2(B)/RG(1.0) sample. Also, the XPS spectrum in the V2p region (Fig. 3c) and the binding energies of $V2p_{3/2}$ and $V2p_{1/2}$ are centered at 516.4 and 523.6 eV, respectively, which is consistent with the characteristic binding energies of V (+4) [41, 42], and further suggests that the VO_2(B) nanobelts was formed in RG composites.

To estimate the amount of RG in the VO_2(B)/RG composite, thermogravimetric analysis (TGA) was carried out in air. As shown in Fig. 4, all the materials show a little mass loss around 100 °C due to the evaporation of absorbed water. In addition, the VO_2(B)/RG composites and bare RG show a little mass loss from around 200 to 300 °C due to the decomposition of oxygen-containing groups that did not restore completely on the graphene. The main weight loss at ~420 °C could be attributed to the oxidation of graphene nanosheets. After 500 °C, the retained mass of the VO_2(B) powder was increased by 4 wt%, which may be ascribed to the transformation of VO_2(B) to V_2O_5 [43]. Meanwhile, the VO_2(B)/RG composites show a rapid mass loss at 420–500 °C as VO_2(B) converses to V_2O_5. The VO_2(B) sample remains stable in the temperature range of 420–700 °C, with no any weight change for the VO_2(B)/RG sample around this temperature range corresponding to the oxidation of RG. Therefore, the difference in weight between VO_2(B) and VO_2(B)/RG after the oxidation could be directly translated into the amount of RG in the VO_2(B)/RG composites. Therefore, the mass ratio of RG in composites estimated by thermal analysis is 4.1, 9.3 and 18.2 wt% for VO_2(B)/RG(0.5), VO_2(B)/RG(1.0) and VO_2(B)/RG(2.0), respectively.

3.2 Morphologies characterization

Figure 5 presents the FESEM images of VO_2(B) (a), RG (b) and VO_2(B)/RG (c–f) composite materials with different RG amounts. As shown in Fig. 5, all samples exhibit a nanobelt-like morphology, where the nanobelts have a

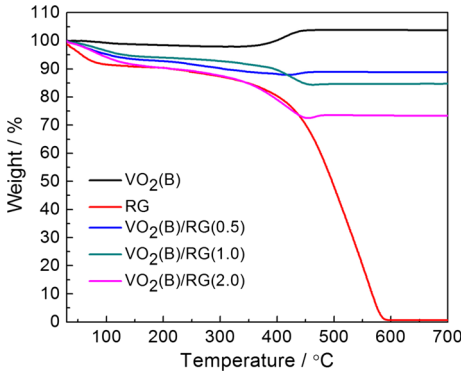

Fig. 4 The thermal gravimetric analysis (TGA) spectrum of pure VO_2(B) and RG,VO_2(B)/RG(0.5), VO_2(B)/RG(1.0), VO_2(B)/RG(2.0)

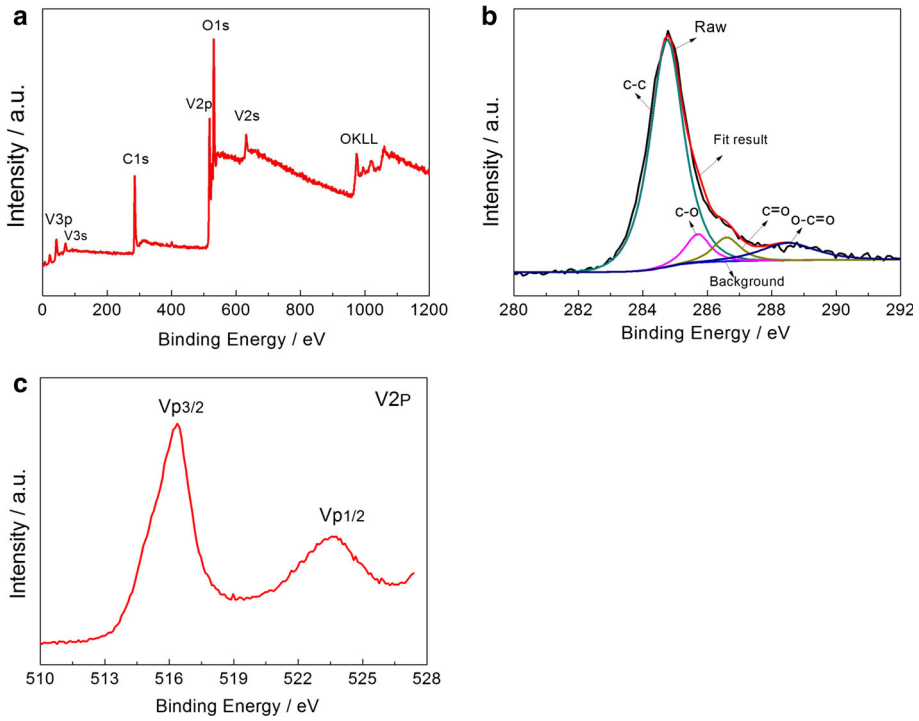

Fig. 3 XPS spectra of the VO_2(B)/RG(1.0) composite: **a** survey scan, **b** C1s region, **c** V2P

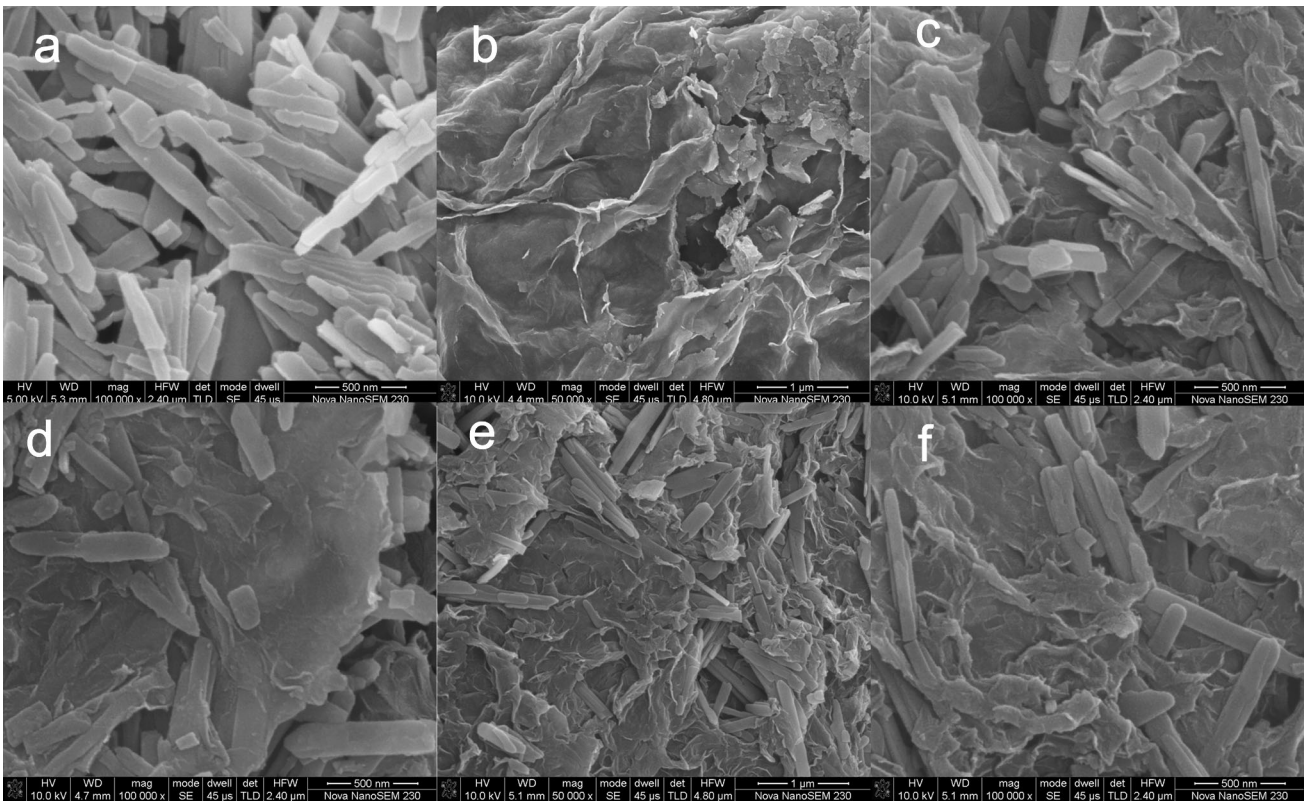

Fig. 5 FESEM images of VO_2(B) (**a**), RG (**b**), VO_2(B)/RG(0.5) (**c**) and VO_2(B)/RG(2.0) (**d**); **e**, **f** FESEM images of VO_2(B)/RG(1.0) at low- and high-magnifications

smooth surface, a typical length of 500–800 nm, width of 80–100 nm. Sample RG (Fig. 5b) shows a plate-like morphology with randomly dispersed and crumpled sheets and closely associated with each other. Compared with the composite materials, the phenomenon of agglomeration is very serious for the pure VO_2(B) (Fig. 5a). In the RG composites, VO_2(B) nanobelts are densely loaded on the graphene layers and some VO_2(B) nanobelts are wrapped up in crumpled micrometer-size graphene layers, demonstrating that the VO_2(B) nanobelts are interwoven with the soft graphene. This unique structure offers easy access to electrolytes as well as facilitating the fast electron transfer, and increasing capacity storage. In company with the increase of RG amounts in the VO_2(B)/RG composites, the agglomeration of VO_2(B) nanobelts are obviously decreased and uniformly loaded on the RG nanosheets, suggesting that the existence of RG nanosheets decreases the agglomeration of VO_2(B) nanobelts.

The typical TEM images of RG composites (Fig. 6a, b) show well-dispersed nanobelts on the graphene layers. The widths of the nanobelts range from 80 to 100 nm, which are consistent with the SEM images. From the HRTEM (Fig. 6c), the lattice fringes are clearly found with a d-spacing of 0.35 nm, corresponding to the (110) planes of VO_2(B) crystals [18, 44].

3.3 Electrochemical properties of VO_2(B)/graphene composites

The capacitive properties of the graphene composites as a supercapacitor electrode material are evaluated by CV and galvanostatic charge–discharge measurements. The CV curves of pure VO_2(B), RG, VO_2(B)/RG(0.5), VO_2(B)/RG(1.0) and VO_2(B)/RG(2.0) electrodes at 5 mV s^{-1} are shown in Fig. 7a. The CV curves of RG show a similar rectangular and symmetrical shape indicating a double-capacitance [45], while the curves of VO_2(B)/RG(0.5), VO_2(B)/RG(1.0), VO_2(B)/RG(2.0) CV deviate from the ideal rectangle, indicating a faradic pseudo-capacitive nature of these electrodes, although no distinct redox peaks were observed on curves [46]. Based on previous studies, the specific capacitance can be calculated by integrating the area under the CV curve to obtain the charge (Q) and divided by the mass of electro-active material (m), the scan rate (v), and the potential window ($\Delta V = V_a - V_c$) according to the following Eq. (1) [40]:

$$C = \frac{Q}{\Delta V} = \frac{1}{mv(V_a - V_c)} \int_{V_c}^{V_a} I(V)\mathrm{d}V \quad (1)$$

The values of specific capacitance at 5 mV s^{-1} are 114.5, 222.3, 283.1, 312.4, and 265.6 F g^{-1} for pure RG,

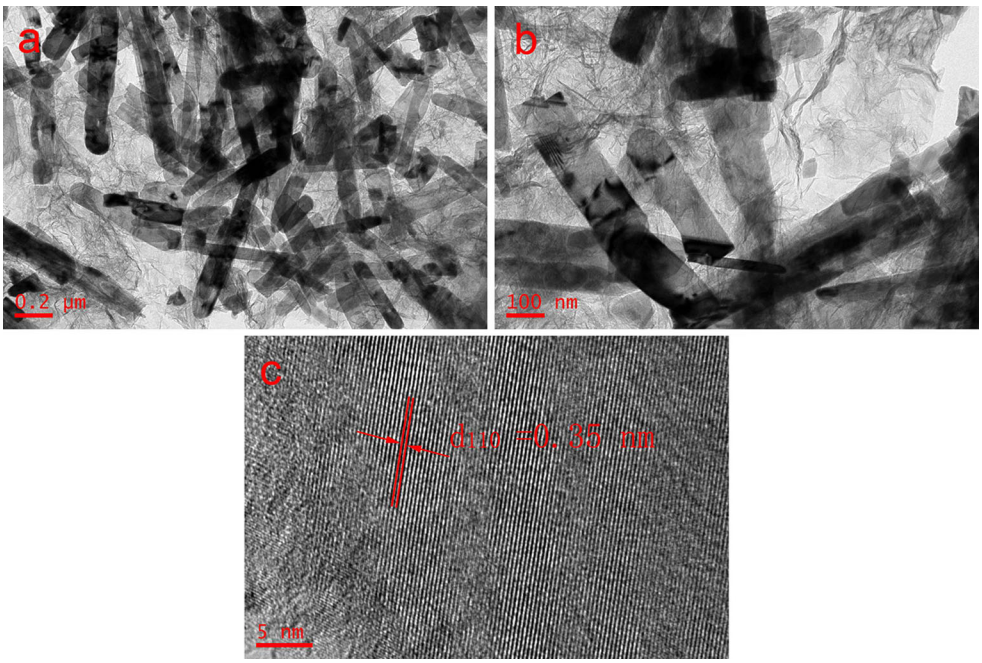

Fig. 6 **a**, **b** The low and high-magnification TEM images of VO_2(B)/RG(1.0), **c** the corresponding HRTEM image of VO_2(B)/RG(1.0)

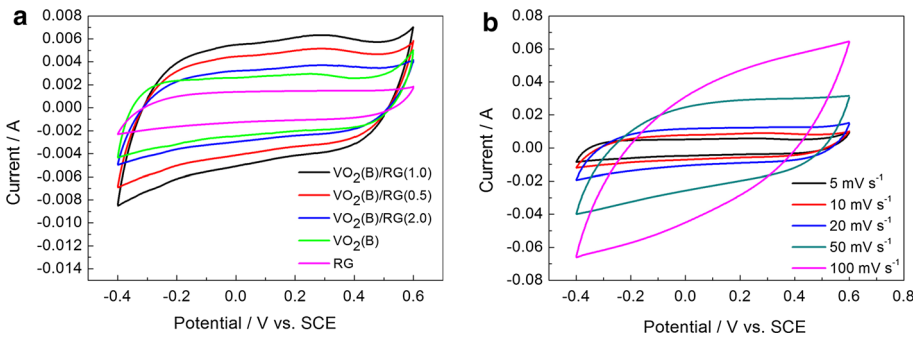

Fig. 7 **a** Cyclic voltammograms of pure VO_2(B), RG, VO_2(B)/RG(0.5), VO_2(B)/RG(1.0), VO_2(B)/RG(2.0) electrodes in 1 M Na_2SO_4 solution at 5 mV s^{-1}; **b** cyclic voltammograms of VO_2(B)/RG(1.0) electrode in 1 M Na_2SO_4 solution at various scan rates

VO_2(B), VO_2(B)/RG(0.5), VO_2(B)/RG(1.0) and VO_2(B)/RG(2.0), respectively. The specific capacitance of RG in 1 M Na_2SO_4 solution could be attributed to the nature of the electrolyte, which provides a double-capacitance [44]. While in RG composites electrode, both graphene and VO_2(B) nanobelts can make electrochemical contributions to its final specific capacitance. Figure 7b shows the CV curves of VO_2(B)/RG(1.0) electrode under different scan rates in 1 M Na_2SO_4 electrolyte. The rectangular shape of the CV curve can be seen even at 50 mV s^{-1} and all of the CV curves are symmetry, indicating the reversibility in the Faraday redox reactions and a good cycle efficiency of the reversibility in the Faraday redox reactions and a good cycle efficiency of the charge–discharge process [47, 48]. The specific capacitance of VO_2(B)/RG(1.0) is 312, 291, 255,202, 141 F g^{-1} at 5, 10, 20, 50, and 100 mV s^{-1}, respectively. The higher specific capacitance of VO_2(B)/RG can be attributed to the improvement of conductivity and better kinetic nature of electrode. Besides, the VO_2(B)/RG(1.0) exhibits the best capacitance performance among three RG composites. We identified the reasons as follows: when the composites is low content of graphene, the conductivity of RG composites cannot be improved effectively. While higher RG concentration would result in a serious agglomeration of active materials, which decreases the specific surface for electrochemical reaction.

In addition, galvanostatic charge–discharge curves of pure VO_2(B), VO_2(B)/RG(0.5), VO_2(B)/RG(1.0) and VO_2(B)/RG(2.0) at 0.2 A g^{-1} are shown in Fig. 8a. The specific capacitance can be calculated from the galvanostatic charging-discharging curves according to the following Eq. (2) [40]:

$$C = \frac{I \times \Delta t}{\Delta V \times m} \tag{2}$$

where C is the specific capacitance, I is the current (A), Δt is the discharging time (s), ΔV is the potential window (V), and m is the mass of electroactive material (g). The

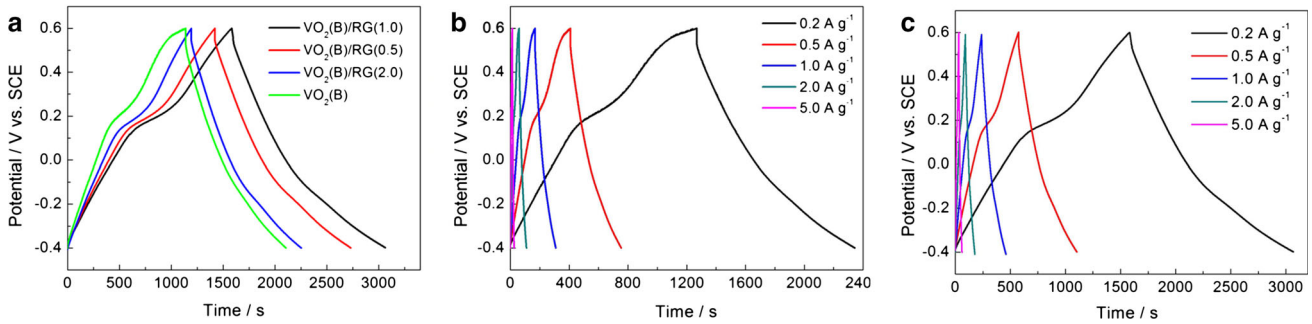

Fig. 8 **a** Galvanostatic discharge curves of pure VO_2(B), VO_2(B)/RG(0.5), VO_2(B)/RG(1.0), VO_2(B)/RG(2.0) electrodes in 1 M Na_2SO_4 solution at 0.2 A g^{-1}; **b, c** galvanostatic charge–discharge curves of pure VO_2(B) and VO_2(B)/RG(1.0) electrode in 1 M Na_2SO_4 solution at different current densities

values of specific capacitance at 0.2 A g^{-1} are 209.2, 254.6, 290.4, and 235.1 F g^{-1} for pure VO_2(B), VO_2(B)/RG(0.5), VO_2(B)/RG(1.0) and VO_2(B)/RG(2.0), respectively, which are consistent with the results of CV measurement. The specific capacitance of pure VO_2(B) is 209.2, 173.9, 142.0, 101.7, and 62.2 F g^{-1} at 0.2, 0.5, 1, 2, and 5 A g^{-1} (Fig. 8b), respectively. Obvious voltage (IR) drop is found at 0.5 A g^{-1}. In contrast, the specific capacitance of VO_2(B)/RG(1.0) is 290.4, 278.5, 245.2, 194.1, and 157 F g^{-1} at 0.2, 0.5, 1, 2 and 5 A g^{-1} (Fig. 8c), respectively. Only a negligible voltage drop is detected even at 1 A g^{-1} at this time. These results indicate that there is a synergistic effect between VO_2(B) nanobelts and RG layers, and it plays an important role in improving the capacitance of the composite. Firstly, the VO_2(B) nanobelts embedded into the RG layers can effectively prevent the agglomeration and stacking of RG layers. In turn, RG layers also prevent the agglomeration and stacking of VO_2(B) nanobelts, resulting in an increasing of the capacitance. Furthermore, this structure is beneficial to the diffusion of the electrolyte during the charge–discharge process, and improves the electrochemical utilization of VO_2(B) nanobelts. Secondly, RG layers in the composite electrode assist in maintaining the mechanical integrality and high electrical conductivity of the overall electrode due to its superior mechanical properties, good conductivity, and excellent electrochemical stability [31].

The electrochemical impendence spectroscopy (EIS) measurement is also complemented at open circuit potential in the frequency range from 0.01 Hz to 100 kHz to investigate the transport characteristics of the charge carries in VO_2(B)/RG(1.0) and pure VO_2(B) electrodes. As shown in Fig. 9, both plots shape of a semicircle at the high frequency region, followed by a relatively linear response at the low frequencies. The initial non-zero intercept at the beginning of the semicircle in high frequency region is similar to the curves which is the result of the electrical resistance of the electrolyte (*R*ele), with about 2.04 Ω. In addition, the charge-transfer resistance of pure VO_2(B) is

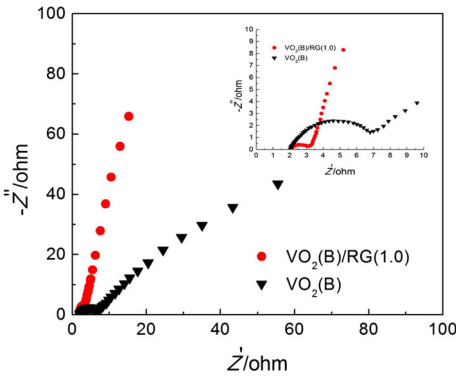

Fig. 9 Nyquist plots for VO_2(B)/RG(1.0) and pure VO_2(B) electrodes

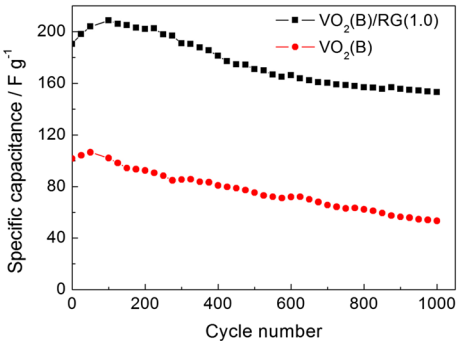

Fig. 10 Cycling performance of VO_2(B)/RG(1.0) and pure VO_2(B) at 2.0 A g^{-1}

about 4.86 Ω, which is much larger than 1.21 Ω of VO_2(B)/RG(1.0), indicating the conductivity of VO_2(B)/RG(1.0) is greatly improved compared to that of pure VO_2(B).

Cycling performance was conducted by repeating galvanostatic charge–discharge test at 2 A g^{-1} for 1000 cycles. After 1000 consecutive cycles, the specific capacitances of VO_2(B) and VO_2(B)/RG(1.0) electrodes are 44.5 and 159.7 F g^{-1}, corresponding to 44.4 and 82.3 % of their initial value, respectively. The improved cycling performance of VO_2(B)/RG(1.0) electrode is

probably due to the reduced graphene oxide, which promoted fast Faradic charge and discharge of the VO_2(B) nanobelts. In addition, this unique structure may solve the aggregation problem of nanoscaled electrode materials during long-term cycles and improve their structural stability (Fig. 10).

4 Conclusion

The VO_2(B)/RG composite in which VO_2(B) nanobelts anchored on graphene layers was prepared for electrochemical capacitors application. Particularly, among the prepared composites, the VO_2(B)/RG(1.0) composite electrode exhibited the highest capacitance of 290.4 F g^{-1} in 1 M Na_2SO_4 at a current density of 0.2 A g^{-1} as well as good rate capability. Such a good electrochemical performance may be ascribed to the unique configuration and a synergistic effect of the combined conductive graphene layers and high pseudo-capacitance of VO_2(B) nanobelts. In addition, the graphene matrix prevented agglomeration of VO_2(B) nanobelts leading to an improved cycle life.

Acknowledgments This work was financially supported by the National Natural Science Foundation of China (No. 81272541).

References

1. P. Simon, Y. Gogotsi, Nat. Mater. **7**, 845–854 (2008)
2. S. Zhou, H. Zhang, Q. Zhao, X. Wang, J. Li, F. Wang, Carbon **52**, 440–450 (2013)
3. F. Xiao, Y.L. Xu, J. Mater. Sci.: Mater. Electron. (2012). doi:10.1007/s10854-012-1034-9. (online first)
4. H.M. Luo, F.B. Zhang, P. Yang, J. Mater. Sci.: Mater. Electron. **24**, 601–606 (2013)
5. C. Liu, F. Li, L.P. Ma, H.M. Cheng, Adv. Mater. **22**, E28–E62 (2010)
6. M. Li, Y.Q. Zhang, L.L. Yang, Y.K. Liu, J.Y. Ma, J. Mater. Sci.: Mater. Electron. (2015). doi:10.1007/s10854-014-2425-x. (online first)
7. E. Frackowiak, F. Beguin, Carbon **39**, 937–950 (2001)
8. A.G. Pandolfo, A.F. Hollenkamp, J. Power Sources **157**, 11–27 (2006)
9. S. Sarangapani, B. Tilak, C.P. Chen, J. Electrochim. Soc. **143**, 3791–3799 (1996)
10. J. Li, X. Wang, Q. Huang, S. Gamboa, P.J. Sebastian, J. Power Sources **158**, 784–788 (2006)
11. C. Zhang, Z. Chen, Z. Guo, X.W. Lou, Energy Environ. Sci. **6**, 974 (2013)
12. Q. Zhao, L. Jiao, W. Peng, H. Gao et al., J. Power Sources **199**, 350–354 (2012)
13. L. Mai, L. Xu, C. Han, X. Xu, Y. Luo, S. Zhao, Y. Zhao, Nano Lett. **10**, 4750–4755 (2010)
14. L.Y. Liang, H.M. Liu, W.S. Yang, J. Alloy. Compd. **559**, 167–173 (2013)
15. X. Pan, Y. Zhao, G.F. Ren, Z.Y. Fan, Chem. Commun. **49**, 3943–3945 (2013)
16. M. Warwick, A. Roberts, R. Slade, R. Binions, J. Mater. Chem. A **2**, 6115–6120 (2014)
17. J.I. Sohn, H.J. Joo, A.E. Porter, C.J. Choi, K. Kim, D.J. Kang, M.E. Welland, Nano Lett. **7**, 1570–1574 (2007)
18. S. Yamamoto, N. Kasai, Y. Shimakawa, Chem. Mater. **21**, 198–200 (2008)
19. S. Zhang, B. Shang, J. Yang, W. Yan, S. Wei, Y. Xie, PCCP **13**, 15873–15881 (2011)
20. J.Y. Suh, R. Lopez, L.C. Feldman, R.F. Haglund, J. Appl. Phys. **96**, 1209 (2004)
21. L. Hu, L. Yu, C. Zhao, X. Long, W. Chen, J. Wuhan Univ. Technol. **25**, 574–578 (2010)
22. C. Nethravathi, B. Viswanath, J. Michael, M. Rajamath, Carbon **50**, 4839–4846 (2012)
23. A.K. Geim, K.S. Novoselov, Nat. Mater. **6**, 183–191 (2007)
24. X. Du, I. Skachko, A. Barker, E.Y. Andrei, Nat. Nanotechnol. **3**, 491–495 (2008)
25. K.I. Bolotin, K. Sikes, Z. Jiang, M. Klima et al., Solid State Commun. **146**, 351–355 (2008)
26. A.A. Balandin, S. Ghosh, W. Bao, I. Calizo, D. Teweldebrhan, F. Miao, C.N. Lau, Nano Lett. **8**, 902–907 (2008)
27. S. Stankovich, D.A. Dikin, G.H. Dommett, K.M. Kohlhaas et al., Nature **442**, 282–286 (2006)
28. G. Yu, L. Hu, M. Vosgueritchian, H. Wang et al., Nano Lett. **11**, 2905–2911 (2011)
29. S.K. Meher, G.R. Rao, J. Phys. Chem. C **115**, 15646–15654 (2011)
30. H. Wang, H.S. Casalongue, Y. Liang, H. Dai, J. Am. Chem. Soc. **132**, 7472–7477 (2010)
31. W. Fan, W. Gao, C. Zhang, W.W. Liu, J. Pan, T. Liu, J. Mater. Chem. **22**, 25108–25115 (2012)
32. L. Deng, G. Zhang, L. Kang, Z. Lei, C. Liu, Z.H. Liu, Electrochim. Acta **112**, 448–457 (2013)
33. W.S. Hummers, R.E. Offeman, J. Am. Chem. Soc. **80**, 1339 (1958)
34. H. Chen, M.B. Müller, K.J. Gilmore, G.G. Wallace, D. Li, Adv. Mater. **20**, 3557–3561 (2008)
35. C. Nethravathi, C.R. Rajamathi, M. Rajamathi, U.K. Gautam, X. Wang, D. Golberg, Y. Bando, ACS Appl. Mater. Int. **5**, 2708–2714 (2013)
36. S. Park, K.S. Lee, G. Bozoklu, W. Cai, S.T. Nguyen, R.S. Ruoff, ACS Nano **2**, 572–578 (2008)
37. H.L. Guo, X.F. Wang, Q.Y. Qian, F.B. Wang, X.H. Xia, ACS Nano **3**, 2653–2659 (2009)
38. Y. Shi, S.L. Chou, J.Z. Wang, H.J. Li, H.K. Liu, Y.P. Wu, J. Power Sources **244**, 684–689 (2013)
39. E. Baudrin, G. Sudant, D. Larcher, B. Dunn, J.M. Tarascon, Chem. Mater. **18**, 4369–4374 (2006)
40. J.W. Lee, A.S. Hall, J.D. Kim, T.E. Mallouk, Chem. Mater. **24**, 1158–1164 (2012)
41. X. Chen, X. Wang, Z. Wang, J. Wan, J. Liu, Y. Qian, Nanotechnology **15**, 1685–1687 (2004)
42. G. Silversmit, H. Poelman, D. Depla, N. Barrett et al., Surf. Interface Anal. **38**, 1257–1265 (2006)
43. M.M. Rahman, J.Z. Wang, N.H. Idris, Z. Chen, H. Liu, Electrochim. Acta **56**, 693–699 (2010)
44. W. Chen, J. Peng, L. Mai, H. Yu, Y. Qi, Solid State Commun. **132**, 513–516 (2004)
45. B. Wang, J. Park, C. Wang, H. Ahn, G. Wang, Electrochim. Acta **55**, 6812–6817 (2010)
46. J. Shao, X. Li, Q. Qu, H. Zheng, J. Power Sources **219**, 253–257 (2012)
47. Y.H. Lin, T.Y. Wei, H.C. Chien, S.Y. Lu, Adv. Eng. Mater. **1**, 901–907 (2011)
48. M. Toupin, T. Brousse, D. Bélanger, Chem. Mater. **14**, 3946–3952 (2002)